REPORT DOCUMENTATION PAGE

1. REPORT DATE (DD-MM-YYYY) 04-15-1998	2. REPORT TYPE Journal Article	3. DATES COVERED (From - To) 1 Oct 96 – 30 Sept 00

4. TITLE AND SUBTITLE	
Magnetically tuned wide-band quantum well infrared photodetectors	**5a. CONTRACT NUMBER**
	5b. GRANT NUMBER
	5c. PROGRAM ELEMENT NUMBER 61102F
6. AUTHOR(S) Danhong Huang, S. K. Lyo	**5d. PROJECT NUMBER** 2305
	5e. TASK NUMBER TJ
	5f. WORK UNIT NUMBER 02

7. PERFORMING ORGANIZATION NAME(S) AND ADDRESS(ES) Air Force Research Laboratory 3550 Aberdeen Ave. SE Kirtland AFB, NM 87117-5776	8. PERFORMING ORGANIZATION REPORT NUMBER

9. SPONSORING / MONITORING AGENCY NAME(S) AND ADDRESS(ES)	10. SPONSOR/MONITOR'S ACRONYM(S)
	11. SPONSOR/MONITOR'S REPORT NUMBER(S)

12. DISTRIBUTION / AVAILABILITY STATEMENT
Approved for Public Release; Distribution is Unlimited.

13. SUPPLEMENTARY NOTES

14. ABSTRACT
The electron eigenstates of double quantum well system in an in-plane magnetic field are calculated accurately using the density-functional theory, which includes the Coulomb interaction between electrons. The absorption coefficient as a function of the probe photon energy is further calculated using the self-consistent-field theory, which takes into account many-body effects on the optical intersubband transitions. The dependence of the absorption spectra on the magnetic field, temperature, electron density, well and middle-barrier widths, quantum-well symmetry, and electric field has been studied extensively. It provides an unconventional approach for designing a tunable wide-band quantum well infrared photodetectors by applying an in-plane magnetic field.

20021212 109

15. SUBJECT TERMS
Magnetic field, density-functional; intersubband; photodetectors

16. SECURITY CLASSIFICATION OF:			17. LIMITATION OF ABSTRACT	18. NUMBER OF PAGES	19a. NAME OF RESPONSIBLE PERSON David Cardimona
a. REPORT Unclassified	b. ABSTRACT Unclassified	c. THIS PAGE Unclassified	Unlimited	10	19b. TELEPHONE NUMBER (include area code) (505) 846-5807

Standard Form 298 (Rev. 8-98)
Prescribed by ANSI Std. 239.18

Magnetically tuned wide-band quantum well infrared photodetectors

Danhong Huang[a)]

Phillips Laboratory (PL/VTMR), 3550 Aberdeen Avenue Southeast, Building 426, Kirtland Air Force Base, New Mexico 87117

S. K. Lyo

Sandia National Laboratories, Albuquerque, New Mexico 87185

The electron eigenstates of double quantum well system in an in-plane magnetic field are calculated *accurately* using the density-functional theory which includes the Coulomb interaction between electrons. The absorption coefficient as a function of the probe photon energy is further calculated using the self-consistent-field theory which takes into account *many-body effects* on the optical intersubband transitions. The dependence of the absorption spectra on the magnetic field, temperature, electron density, well and middle-barrier widths, quantum-well symmetry, and electric field has been studied extensively. It provides an unconventional approach for designing a tunable wide-band quantum well infrared photodetector by applying an in-plane magnetic field. [S0021-8979(98)04108-5]

I. INTRODUCTION

Quantum well infrared photodetectors based on III-V semiconductors have been studied in recent years as alternative structures to replace II-VI semiconductor materials in the infrared focal-plane arrays FPAs technology. According to the Planck's black-body radiation law, each object with fixed temperature will radiate with a characteristic wavelength at which the radiation will reach its maximum. The higher the temperature is, the longer the wavelength will be. In other words, a certain temperature distribution of the imaged object gives rise to a wide-band emission spectrum. In this sense, the wide-band or multicolor infrared photodetectors are needed for the best thermal imaging recognition. In fact, one can extract many useful details from images obtained using FPAs with wide-band or multicolor spectra.

There have been many efforts devoted to the fabrication of multicolor infrared photodetectors. The simplest method is to construct an image with multi-FPAs each covering a different spectral band. Another method is to grow multistacks of different quantum well photodetector structures separated by thick doped layers for different electrical contacts.[1-4] However, the existence of too many electrodes greatly complicates the device processing and the read-out electronics. Two-terminal devices have also been tested,[5,6] where the detected wavelength can be switched by applying different bias voltages. Due to the in-series electrical connections in this structure, a spectral crosstalk occurs when different stacks are illuminated simultaneously in different wavelengths. The quantum confined Stark shift has been used to tune the detection wavelength by varying the bias voltage.[7-10] Unfortunately, the operation of these structures usually requires a relatively high bias voltage causing a large dark current and noise. The stack of a quantum well photodetector and a photodiode[11] can operate in a long wavelength

photodetector absorption mode or in a short wavelength photodiode absorption mode by applying a forward or a reverse bias voltages. However, this structure depends on the bias voltage and requires three electrical contact layers. It again complicates the device processing and introduces image distortions in the continuous operation mode. The multi-subband quantum well photodetector[12-15] has more than one occupied subband, and the multi-intersubband transitions take place between the occupied subbands or between occupied subband and a top empty subband. However, it is very difficult to design for the detection of more than three colors in this kind of structure.

The energy of the interband transition between a conduction and a valence subband in quantum wells increases with the electron wavevector. It gives rise to a wide-band absorption[16] after summing over all the available electron states. This is because the dispersion of the electron subband is upward, while that of the valence subband is downward. In contrast, the intersubband transitions are sharp because all the electron subbands in the conduction band have the same parabolic dispersion relation determined by the electron effective mass. The known nonparabolic effects include the k dependence of the electron effective mass[15] due to the nonparabolicity in the well or barrier bulk materials, the subband-index dependent electron effective mass[14] due to different electron effective masses in the well and barrier material, and the nonparabolic electron energy dispersion due to the exchange interaction[14,15] between electrons. However, all these effects are far too small to produce a wide-band transition.

In this article, we study the optical transition between the states in the two lowest conduction subbands of the double quantum wells. It is now well known that the electron subband dispersion in the double quantum wells can be greatly modified by applying a parallel magnetic field to the system.[17,18] The main effect of the in-plane (i.e., parallel) magnetic field is to displace the energy-dispersion parabolas
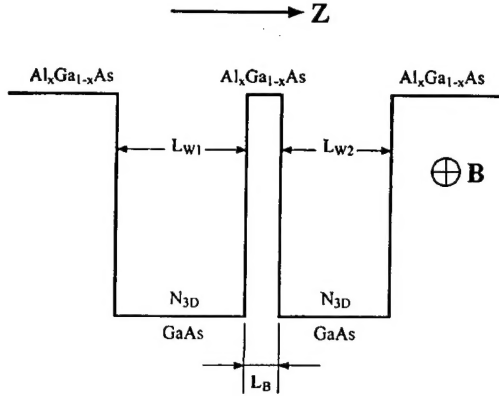
[a)]Electronic mail: huangd@plk.af.mil

FIG. 1. Sketch of the double quantum well model in which well material is GaAs and barrier material is $Al_xGa_{1-x}As$, left well width is L_{W1}, middle barrier thickness is L_B, and right well width is L_{W2}. The doping is uniform and only in the well region with concentration N_{3D}, and the parallel magnetic field **B** is in the x direction parallel to the plane quantum wells.

of the double quantum wells sketched in Fig. 1 in the transverse direction in k space by an amount proportional to the parallel magnetic field. The displaced parabolas anticross due to the electron tunneling between the two quantum wells, opening a partial energy gap, as shown in Fig. 2. As the parallel magnetic field is increased, the gap passes through the chemical potential. When the double quantum wells are doped with electrons, the shape of the Fermi-energy surface in k space strongly depends on the magnitude of the parallel magnetic field. There exists a logarithmic singularity in the density-of-states at the saddle point of the lower gap edge when the parallel magnetic field is strong enough. Since the elastic scattering of electrons occurs only on the Fermi-energy surface, which conserves the electron energy, a strong modification of the electron elastic scattering is expected[18] by varying the strength of the parallel mag-
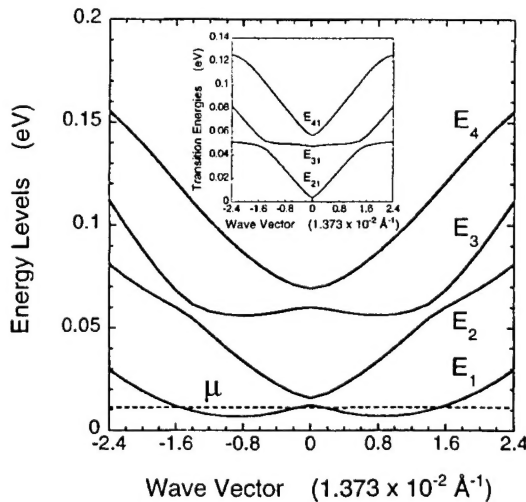

FIG. 2. The energy levels $E_j(k_y)$ with $j=1, 2, 3, 4$ as a function of the electron wave vector k_y at $B=9.0$ T. The dashed line represents μ which is the chemical potential of the system. The inset shows the transition energies $E_{j'j}(k_y)$ with $j'=2, 3, 4$ and $j=1$ as a function of k_y at $B=9.0$ T. In our numerical calculation, we have chosen: $x=0.30$, $E_{dc}=0$, $T=4.0$ K, $N_{3D}=2.0\times10^{17}$ cm^{-3}, $L_{W1}=L_{W2}=150$ Å, and $L_B=20$ Å.

netic field. Therefore, the electron dc-transport at low temperatures can be controlled by the parallel magnetic field because the transport itself is mainly determined by the electron density-of-states and electron velocities at the Fermi energy.[17,18]

For the optical transition, all the occupied electron states contribute to this process. The bandwidth of the infrared photodetection is directly determined by the dispersion of the transition energy between two electron subbands. From previous works as well as our calculations we know that sharp intersubband transitions in the double quantum wells at zero magnetic field change into wide-band transitions when a parallel magnetic field is applied to the system. Therefore, an unconventional approach is proposed in this article for designing the wide-band quantum well infrared photodetectors by applying a parallel magnetic field, in which both the bandwidth and the strength of the windowlike infrared absorption spectra can be controlled by the parallel magnetic field. There are some reports on the Coulomb interaction effect on the magneto transport of electrons in coupled double quantum wells[19] and wide single quantum wells[20] when a parallel magnetic field is applied. Our current work has generalized the previous approximate calculation of the electron eigenstates[17,18] which used the *nearest-neighbor tight-binding* model into an accurate calculation of electron eigenstates for double quantum wells in a parallel magnetic field using the density-functional theory with the inclusion of the Coulomb interaction between electrons, z dependence of electron effective mass and dielectric constant, nonparabolic effect, and a static electric field. The calculated absorption coefficient based on results from the density-functional theory has taken into account the many-body effects which was neglected in the previous *single-particle response theory.*[21]

This article is organized as follows. In Sec. II, the electron eigenstates in double quantum wells under a parallel magnetic field will be calculated accurately by using the density-functional theory including the Coulomb interaction between electrons, z dependence of electron effective mass and dielectric constant, nonparabolic effect, and a static electric field. In Sec. III, we will use the self-consistent-field theory to calculate the absorption coefficient as a function of the probe photon energy including the many-body effects. The numerical results of the optical intersubband absorption spectra will be presented in Sec. IV with various magnetic fields, temperatures, electron densities, well widths, middle-barrier widths, quantum-well symmetries, and electric fields. Finally, the conclusion is presented in Sec. V.

II. SELF-CONSISTENT ELECTRON EIGENSTATES

The model we consider here consists of double quantum wells (DQWs), as shown schematically in Fig. 1, with individual well widths L_{W1} and L_{W2}. The two quantum wells are separated by a middle barrier layer with thickness L_B. The well material is assumed to be GaAs and the barrier material is $Al_xGa_{1-x}As$. The electrons are uniformly doped within each quantum well with individual electron density n_{2D}^1 and n_{2D}^2. A magnetic field **B** is applied to the system in the di-

rection parallel to the plane of the quantum wells. The Schrö-dinger equation which determines the wavefunction $\phi_{jk_y}(z)$ and energy level $E_j(k_y)$ in the density-functional theory is

$$\left\{ -\frac{\hbar^2}{2}\frac{d}{dz}\left[\frac{1}{m^*(z)}\frac{d}{dz}\right] + V_{\text{DQW}}(z) + eE_{\text{dc}}z \right.$$

$$+\frac{\hbar^2}{2m^*(z)}\left(k_y - \frac{z}{l^2}\right)^2 + V_H(z) + V_{\text{XC}}[n(z)]\left.\right\}$$

$$\times \phi_{jk_y}(z) = E_j(k_y)\phi_{jk_y}(z). \qquad (1)$$

In Eq. (1), z is in the quantum-well growth direction, $j = 1, 2, 3,...$ is the subband index, k_y is the electron wave vector in the y direction, $m^*(z)$ is m_W and m_B for well and barrier materials, $V_{\text{DQW}}(z)$ is the double-quantum-well potential profile, E_{dc} is the static electric field applied in the z direction, $\mathbf{B}$ is the magnetic field applied in the x direction with the *Landau gauge* for its vector potential $\mathbf{A} = (0, -Bz, 0)$, and $l = \sqrt{\hbar/eB}$ is the magnetic length. Under the *Landau gauge*, the in-plane part of the electron wave function is kept as a plane wave. The Coulomb interaction between electrons is represented by the sum of the Hartree and exchange-correlation potentials $V_H(z) + V_{\text{XC}}[n(z)]$. The electron energy is given by

$$E_j(k_x, k_y) = E_j(k_y) + \frac{\hbar^2 k_x^2}{2m_j^*(k_x, k_y)}, \qquad (2)$$

where k_x is the electron wave vector in the x direction, and the nonparabolic effect has been included. Considering that the effective mass of electrons in the well and barrier materials is different, we obtain an "average" effective mass of electrons in the jth subband of DQWs by using the first-order perturbation theory[14]

$$\frac{1}{m_j^*(k_x, k_y)} = \frac{P_j(k_y)}{m_j^W(k_x, k_y)} + \frac{1 - P_j(k_y)}{m_j^B(k_k, k_y)}, \qquad (3)$$

where $P_j(k_y)$ is the dwelling probability of electrons in the well region

$$P_j(k_y) = \int_{\text{Well Region}} [\phi_{jk_y}(z)]^2 dz. \qquad (4)$$

In Eq. (3) $m_j^W(k_x, k_y)$ and $m_j^B(k_x, k_y)$ are the electron effective masses in the well and barrier bulk materials, which include the nonparabolic effect and are given by[22]

$$\frac{m_e}{m_j^\beta(k_x, k_y)} = 1 + \frac{E_P^\beta}{3}\left[\frac{2}{E_G^\beta + E_j(k_y) + \hbar^2 k_x^2/2m_\beta}\right.$$

$$+ \frac{1}{E_G^\beta + \Delta_0^\beta + E_j(k_y) + \hbar^2 k_x^2/2m_\beta}\left.\right], \qquad (5)$$

where m_e is the free electron mass, m_β with $\beta = W, B$ are the Γ-point electron effective mass at $(k_x, k_y, k_z) = 0$ for well and barrier bulk materials, E_P^β is the interband Kane matrix element, E_G^β is the energy gap, and Δ_0^β is the spin-orbit splitting.

The Hartree potential, $V_H(z)$, in Eq. (1) is decided from Poisson's equation

$$\frac{d}{dz}\left[\epsilon_s(z)\frac{d}{dz}V_H(z)\right] = 4\pi e^2[N_D(z) - n(z)], \qquad (6)$$

where $\epsilon_s(z) = 4\pi\epsilon_0\epsilon_b(z)$ depending on z, $\epsilon_b(z)$ is the dielectric constant which takes ϵ_W for the well and ϵ_B for the barrier materials. The doping profile $N_D(z)$ is N_{3D} inside the well and zero outside the well, where N_{3D} is the doping concentration. The exchange-correlation potential, $V_{\text{XC}}[n(z)]$, in Eq. (1) in the local-density approximation is written as[23]

$$V_{\text{XC}}[n(z)] = -\frac{e^2}{8\pi\epsilon_0\epsilon_b(z)a_0^*(z)}\left\{1 + \frac{0.7734 r_s(z)}{21}\right.$$

$$\times \ln\left[1 + \frac{21}{r_s(z)}\right]\left.\right\}\left[\frac{2}{\pi\alpha r_s(z)}\right], \qquad (7)$$

where we have introduced the following notations:

$$\alpha = \left(\frac{4}{9\pi}\right)^{1/3}, \qquad (8)$$

$$a_0^*(z) = \frac{4\pi\epsilon_0\epsilon_b(z)\hbar^2}{m^*(z)e^2} \qquad (9)$$

is the effective Bohr radius for electrons in DQWs, and

$$r_s(z) = \left\{\frac{4}{3}\pi[a_0^*(z)]^3 n(z)\right\}^{-1/3} \qquad (10)$$

is the dimensionless electron density parameter. The electron density function, $n(z)$, is calculated as

$$n(z) = \frac{2}{A}\sum_j \sum_{k_x, k_y} [\phi_{jk_y}(z)]^2 f_0[E_j(k_x, k_y)], \qquad (11)$$

where A is the cross-sectional area of the sample, and $f_0[E_j(k_x, k_y)]$ is the Fermi–Dirac distribution function for the electrons in the equilibrium state

$$f_0[E_j(k_x, k_y)] = \left[\exp\left(\frac{E_j(k_x, k_y) - \mu}{k_B T}\right) + 1\right]^{-1}. \qquad (12)$$

Here, T is the electron temperature, μ is the chemical potential which is decided selfconsistently by the total electron density, n_{2D}, through the charge neutrality condition:

$$n_{2D} = \sum_{j=1}^{2} n_{2D}^j = \int_{-\infty}^{+\infty} n(z)dz$$

$$= \int_{-\infty}^{+\infty} N_D(z)dz = \frac{2}{A}\sum_j \sum_{k_x, k_y} f_0[E_j(k_x, k_y)]. \qquad (13)$$

The electron eigenstates must be self-consistently calculated by solving Eqs. (1)–(13), simultaneously. In this work, we employ the finite-difference method in the numerical calculation, which is combined with the proper boundary conditions. By using this approach, the Schrodinger equation in Eq. (1) has been divided into a tridiagonal matrix eigenvalue and eigenvector problem, while Poisson's equation in Eq. (6) has become an inhomogeneous linear matrix equation with a tridiagonal coefficient matrix. Compared with the previous nearest-neighbor tight-binding model[17–19] which can be ap-

plied only to the zero electric field, weak magnetic field, thick middle-barrier layer and single band situations, the current density-functional theory does not suffer from these limitations and provides the accurate electron eigenstates of the system, even including the Coulomb interaction between electrons, z dependence of electron effective mass and dielectric constant, nonparabolic effect, and a static electric field.

III. MANY-BODY EFFECTS ON OPTICAL ABSORPTION

When an external z-polarized probe field is applied to the system, it causes a perturbation to the electron density function and produces a density fluctuation as an optical response. In the long wavelength limit, we need consider only the vertical intersubband transition. If the probe field is interacting weakly with the electrons in DQWs, the intersubband absorption coefficient can be calculated from the Fermi golden rule. A straightforward calculation yields[14]

$$\beta_{\text{abs}}(\omega) = \frac{\omega\sqrt{\epsilon_b}}{cn(\omega)}[\rho_{\text{ph}}(\omega)+1]\text{Im }\alpha_L(\omega), \quad (14)$$

where ω is the frequency of the probe field, $\epsilon_b = (\epsilon_W + \epsilon_B)/2$,

$$\rho_{\text{ph}}(\omega) = \left[\exp\left(\frac{\hbar\omega}{k_BT}\right)-1\right]^{-1} \quad (15)$$

is the photon distribution factor, and

$$\alpha_L(\omega) = -\frac{e^2}{2\pi\epsilon_0\epsilon_b L_S}\sum_{j,j'}\int_{-\infty}^{+\infty}dk_y F_{j'j}(k_y)[F_{jj'}(k_y)$$
$$+ D_{jj'}^C(k_y,\omega)]\chi_{jj'}(k_y,\omega), \quad (16)$$

is the *Lorentz ratio*, where $L_S = L_{W1} + L_{W2} + L_B$. The refractive index function in Eq. (14) is also obtained from the *Lorentz ratio* by

$$n(\omega) = \frac{1}{\sqrt{2}}\{1+\text{Re }\alpha_L(\omega)$$
$$+ \sqrt{[1+\text{Re }\alpha_L(\omega)]^2+[\text{Im }\alpha_L(\omega)]^2}\}^{1/2}. \quad (17)$$

The bare dipole moment, $F_{jj'}(k_y)$, in Eq. (16) is found to be

$$F_{jj'}(k_y) = F_{j'j}(k_y) = \int_{-\infty}^{+\infty}\phi_{jk_y}(z)z\phi_{j'k_y}(z)dz, \quad (18)$$

and the polarizability, $\chi_{jj'}(k_y,\omega)$, is

$$\chi_{jj'}(k_y,\omega)$$
$$= \frac{2}{\pi}\int_0^{+\infty}dk_x\left[\frac{f_0[E_j(k_x,k_y)]-f_0[E_{j'}(k_x,k_y)]}{\hbar\omega-E_{j'}(k_x,k_y)+E_j(k_x,k_y)+i\gamma}\right.$$
$$\left.+\frac{f_0[E_{j'}(k_x,k_y)]-f_0[E_j(k_x,k_y)]}{\hbar\omega-E_j(k_x,k_y)+E_{j'}(k_x,k_y)+i\gamma}\right], \quad (19)$$

where γ is the homogeneous broadening factor for the intersubband transition, which is set to be 1.0 meV for our numerical calculation. The many-body effects on the optical absorption is represented by the frequency-dependent collec-

tive dipole-moment, $D_{jj'}^C(k_y,\omega)$. For $n<n'$, it is given by the following matrix equation by using the self-consistent-field therory[24,25]

$$\frac{1}{2\pi}\sum_{j<j'}\int_{-\infty}^{+\infty}dk_y D_{jj'}^C(k_y,\omega)[\delta_{n,j}\delta_{n',j'}\delta(k_y-k_y')$$
$$-\chi_{jj'}(k_y,\omega)U_{nn',jj'}(k_y',k_y)]$$
$$=\frac{1}{2\pi}\sum_{j<j'}\int_{-\infty}^{+\infty}dk_y\chi_{jj'}(k_y,\omega)U_{nn',jj'}(k_y',k_y)F_{jj'}(k_y), \quad (20)$$

where the Coulomb interaction matrix, $U_{nn',jj'}(k_y',k_y)$, is given by

$$U_{nn',jj'}(k_y',k_y) = \int_{-\infty}^{+\infty}dz\int_{-\infty}^{+\infty}dz'\phi_{nk_y'}(z)\phi_{n'k_y'}(z)$$
$$\times\left(-\frac{e^2}{2\epsilon_0\epsilon_b}\left|z-z'\right|\right)\phi_{j'k_y}(z')\phi_{jk_y}(z')$$
$$+\int_{-\infty}^{+\infty}dz\,\phi_{nk_y'}(z)\phi_{n'k_y'}(z)$$
$$\times\left(\frac{\delta V_{\text{XC}}[n(z)]}{\delta n(z)}\right)\phi_{j'k_y}(z)\phi_{jk_y}(z). \quad (21)$$

The coefficient matrix in Eq. (20) is called the dielectric-function matrix. The Coulomb interaction matrix in Eq. (21) contains both the repulsive Hartree interaction and attractive exchange-correlation interaction. When $V_H(z)$, $V_{\text{XC}}[n(z)]$, and $D_{jj'}^C(k_y,\omega)$ are all set to zero, we get the simplified results in the *single-particle response theory*. The previous single-particle response theory,[19] which neglects the collective dipole moment $D_{jj'}^C(k_y,\omega)$ and the k_y dependence in the bare dipole-moment $F_{jj'}(k_y)$, will miss the fine features in the line shape and predicts a down-shifted peak position in the optical absorption spectrum. However, the current theory avoids all these drawbacks.

IV. NUMERICAL RESULTS AND DISCUSSIONS

The numerical results of $\beta_{\text{abs}}(\omega)$ as a function of the photon energy $\hbar\omega$ in Eq. (14) will be presented in this section for various magnetic fields, temperatures, electron densities, well and middle barrier widths, quantum-well symmetries, and electric fields to study the role played by these parameters in the infrared photodetection characteristics of the double quantum well system shown schematically in Fig. 1.

A. Effects of magnetic and electric fields

Figure 2 shows the energy levels $E_j(k_y)$ as a function of the wave vector k_y at $B = 9.0$ T. The unusual energy dispersion seen here can be understood as the result of the coupling of the parabolas in the two quantum wells. In the absence of electron tunneling, there are two parabolas for ground and first excited states in each quantum well. The ground and first excited state parabolas in different quantum wells have minima at $k_y=0$ when $B=0$. Besides, $E_1(k_y)$ and $E_3(k_y)$ states are the even-parity states at $B=0$, while $E_2(k_y)$ and
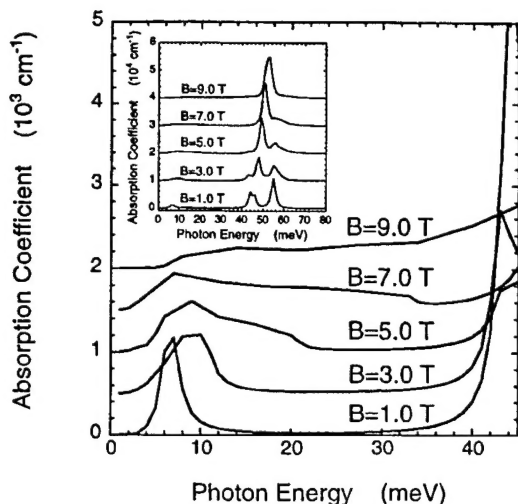
FIG. 3. The enlarged low-energy part of the absorption coefficients $\beta_{abs}(\omega)$ as a function of the photon energy $\hbar\omega$ for magnetic fields $B = 1.0, 3.0, 5.0,$ 7.0, and 9.0 T. The figure is displayed by a vertical shift 0.5×10^3 cm^{-1}. The complete displayed absorption spectra are presented in the inset by a vertical shift 1.0×10^4 cm^{-1}. In our numerical calculation, we have chosen: $x = 0.30$, $E_{dc} = 0$, $T = 4.0$ K, $N_{3D} = 2.0 \times 10^{17}$ cm^{-3}, $L_{W1} = L_{W2} = 150$ Å, $L_B = 20$ Å, and $\gamma = 1.0$ meV.
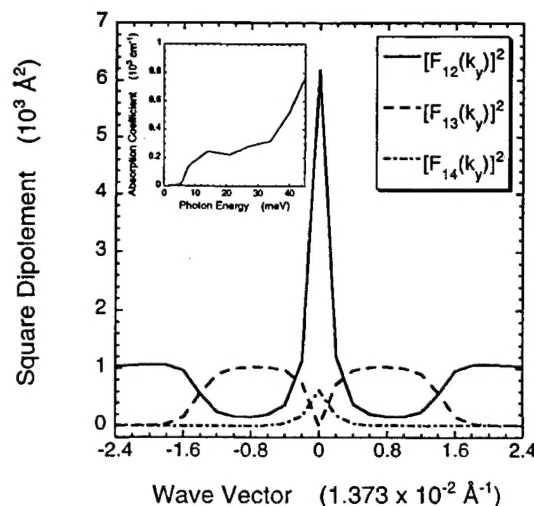

FIG. 4. The square dipole-moments $[F_{12}(k_y)]^2$ (solid curve), $[F_{13}(k_y)]^2$ (dashed curve), and $[F_{14}(k_y)]^2$ (dashed-dotted curve) as a function of k_y at $B = 9.0$ T. The inset displays the enlarged low-energy part of the absorption spectrum reproduced from Fig. 3 for $B = 9.0$ T. The parameters in the calculation are the same as those in Fig. 3.

$E_4(k_y)$ states are the odd-parity states. However, when the parallel magnetic field is applied both the ground and first excited state parabolas in different quantum wells shift their minimas to the opposite values of k_y away from $k_y = 0$, causing the anticrossing among the four parabolas.[18] This introduces a very large dispersion of the transition energies $E_{j'j}(k_y)$, as shown in the inset. From Fig. 2 we also see there is an unpopulated "island" above the chemical potential "sea" (indicated by the dashed line) in the range of $|k_y| \leqslant 0.1$ (in the unit of 1.373×10^{-2} Å^{-1}) for this electron density at $B = 9.0$ T. The electrons can only populate the sea states between $0.1 \leqslant k_y \leqslant 1.5$ or $-1.5 \leqslant k_y \leqslant -0.1$. With this population range for k_y it is easy to see from the inset that the gap between the transition energies $E_{21}(k_y)$ and $E_{31}(k_y)$ and the gap between the transition energies $E_{31}(k_y)$ and $E_{41}(k_y)$ are all closed.

Figure 3 presents the absorption spectra which are displayed for various magnetic fields B. In the inset, we find four absorption peaks when $B = 1.0$ T, which, from left to right, are found to be the transitions from $E_1(k_y)$ to $E_2(k_y)$, $E_2(k_y)$ to $E_3(k_y)$, $E_1(k_y)$ to $E_3(k_y)$, and $E_1(k_y)$ to $E_4(k_y)$, respectively. The transition from $E_2(k_y)$ to $E_3(k_y)$ is gradually suppressed by B, while the transition from $E_1(k_y)$ to $E_3(k_y)$, forbidden at $B = 0$, is enhanced by B at the same time. From the inset we also find that the peak strength of the transition from $E_1(k_y)$ to $E_4(k_y)$ is decreased with B, and the gap between this transition and the transition from $E_1(k_y)$ to $E_3(k_y)$ is reduced and finally closed at $B = 9.0$ T. In the main part of Fig. 3, we enlarge the low-energy part of the absorption spectra to highlight the transition from $E_1(k_y)$ to $E_2(k_y)$, in which we find this transition with a windowlike profile is broadened with increasing B and its absorption strength is decreased simultaneously. Meanwhile, the gap between this transition and the transition from $E_1(k_y)$ to

$E_3(k_y)$ is decreased with B and completely closed at $B = 9.0$ T. At $B = 9$ T, both the transitions from $E_1(k_y)$ to $E_2(k_y)$ and $E_1(k_y)$ to $E_4(k_y)$ for $|k_y| < 1.6$ are interwell transition with transition energies $E_{21}(k_y)$ and $E_{41}(k_y)$ with a large dispersion as seen in the inset of Fig. 2. On the other hand, the transition from $E_1(k_y)$ to $E_3(k_y)$ is intrawell transition with a sharp transition energy $E_{31}(k_y)$ in the range of $|k_y| < 1.6$. The dispersive interwell transition energy $E_{21}(k_y)$ is responsible for the wide-band absorption shown in the main part of Fig. 3. However, the optical absorption is still dominated by the nondispersive intrawell transition from $E_1(k_y)$ to $E_3(k_y)$, which is forbidden at $B = 0$ due to the same parity of the initial and final states in the transition. The findings in Fig. 3 provide us with an unconventional approach for designing a wide-band quantum well infrared photodetector by applying a parallel magnetic field. It has the advantage of very wide bandwidth and windowlike profile for the infrared photodetection over previous conventional approaches.[1–15]

Figure 4 displays the square dipole moments $[F_{jj'}(k_y)]^2$ of the transitions from the ground state to the first, second, and third excited states as a function of the wave vector k_y at $B = 9.0$ T. A strong k_y dependence can be seen. At $k_y = 0$, the potential of the DQWs system is symmetric even under a parallel magnetic field. Therefore, the transition from $E_1(k_y)$ to $E_3(k_y)$ is forbidden, while the transitions from $E_1(k_y)$ to $E_2(k_y)$ and $E_1(k_y)$ to $E_4(k_y)$ are both allowed at $k_y = 0$. The saturation of the square dipole moments $[F_{12}(k_y)]^2$ at large $|k_y| > 1.8$ arises from the fact that the transition $E_1(k_y)$ to $E_2(k_y)$ switches from the interwell to intrawell transition. This saturation is accompanied by the suppression of the square dipole moments $[F_{13}(k_y)]^2$ and $[F_{14}(k_y)]^2$ which correspond to the interwell transitions when $|k_y| > 1.8$. The inset shows the low-energy part of the absorption spectrum at $B = 9.0$ T (reproduced from Fig. 3 for $B = 9.0$ T) in which we find there is a dip around $\hbar\omega = 20$ meV. From the inset of
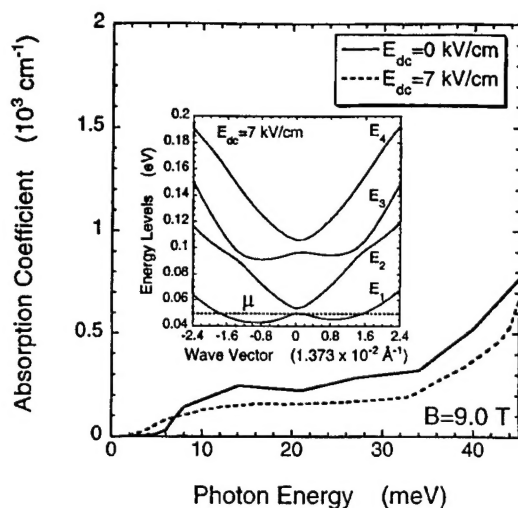
FIG. 5. The comparison of the enlarged low-energy part of the absorption spectra at $B = 9.0$ T for $E_{dc} = 0$ (solid curve) and $E_{dc} = 7$ kV/cm (dashed curve). The energy levels $E_j(k_y)$ with $j = 1, 2, 3, 4$ as a function of the k_y at $B = 9.0$ T for $E_{dc} = 7$ kV/cm is shown in the inset, where μ (dashed line) is the chemical potential of the system. The other parameters in the calculation are the same as those in Fig. 3.

FIG. 6. The comparison of the enlarged low-energy part of the absorption spectra at $B = 9.0$ T between the full theory in this article (solid curve) and the simplified single-particle response theory (dashed curve). The comparison of the complete displayed absorption spectra are presented in the inset by a vertical shift 1.0×10^4 cm^{-1}. The other parameters in the calculation are the same as those in Fig. 3.

Fig. 2 we know that transition energy $E_{21}(k_y) = 20$ meV corresponds to the intersubband transition at $k_y = 0.8$, where $[F_{12}(k_y)]^2$ has a minima in Fig. 4. This is the reason for the occurring of the dip in the inset.

Figure 5 presents the comparison of the absorption spectra for the cases with $E_{dc} = 0$ and $E_{dc} = 7$ kV/cm at $B = 9.0$ T. As an electric field is applied, the low-energy edge of the transition from $E_1(k_y)$ to $E_2(k_y)$ is pushed down in Fig. 5. This can be explained by the fact that the whole energy level dispersion is tilted by the electric field, as shown in the inset, which makes the unpopulated "island" disappear.

B. Comparison between single-particle and full theories

In order to estimate the effect of Coulomb interaction between electrons on the absorption spectrum, we present in Fig. 6 the comparison of the results from our full theory and single-particle response theory in which $D_{jj'}^C(k_y, \omega)$, $V_H(z)$, and $V_{XC}[n(z)]$ are all set to zero. From the inset we find the Coulomb interaction shifts up the absorption peak for the transition from $E_1(k_y)$ to $E_3(k_y)$ by about 4 meV in this case. It also shifts up the low-energy edge of the transition from $E_1(k_y)$ to $E_2(k_y)$ as seen in the main part of the figure. Meanwhile, the absorption strength is brought down by the Coulomb interaction for the wide-band transition from $E_1(k_y)$ to $E_2(k_y)$. When the many-body effect, $D_{jj'}^C(k_y, \omega)$, is included, the absorption will reach its maximum at the *plasmon* energy,[24] instead of the single-particle energy level separation $E_{j'j}(k_y)$ due to the electron screening. The difference between the plasmon energy and $E_{j'j}(k_y)$ is positive and called the *depolarization shift*. This justifies the importance of our using the full theory instead of the single-particle response theory in designing a tunable wide-band quantum well infrared photodetector.
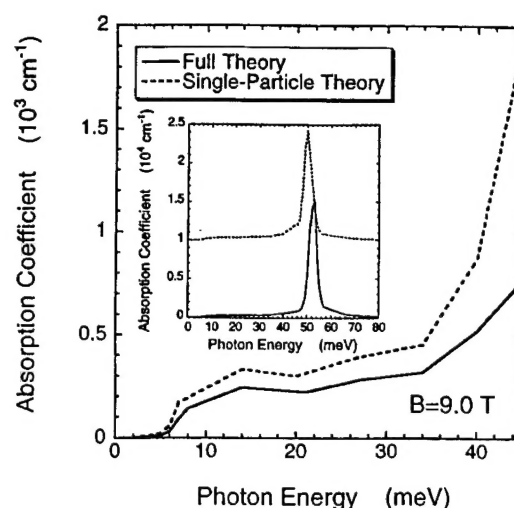
C. Effects of temperature and electron density

Figure 7 displays the absorption spectra for different temperatures, $T = 4$ and 77 K at $B = 9.0$ T. As T is raised from 4 to 77 K, the unpopulated island in the main part of Fig. 2 will be thermally populated. This shifts down the low-energy edge of the transition from $E_1(k_y)$ to $E_2(k_y)$ by about 4 meV as seen in the figure. There is no shifting of the absorption peak for the transition from $E_1(k_y)$ to $E_3(k_y)$ as seen in the inset, except that the peak is slightly broadened as a result of partially populating the electron states with $|k_y| > 1.5$ at $T = 77$ K.
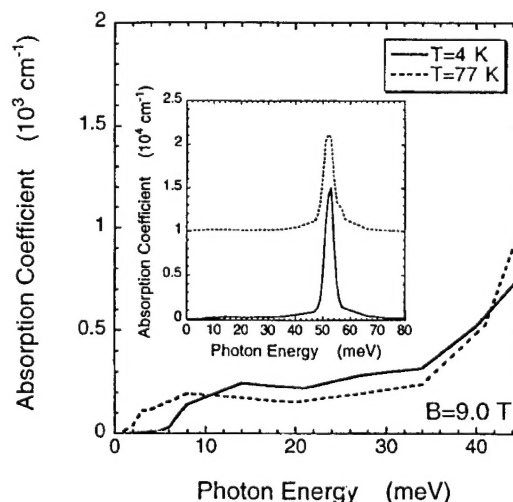

FIG. 7. The comparison of the enlarged low-energy part of the absorption spectra at $B = 9.0$ T for $T = 4$ K (solid curve) and $T = 77$ K (dashed curve). The comparison of the complete displayed absorption spectra are presented in the inset by a vertical shift 1.0×10^4 cm^{-1}. The other parameters in the calculation are the same as those in Fig. 3.
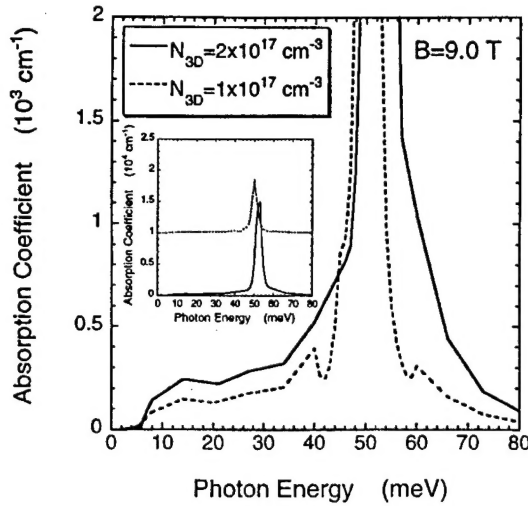
FIG. 8. The comparison of the absorption spectra with an amplified scale at $B=9.0$ T for $N_{3D}=2.0\times10^{17}$ cm^{-3} (solid curve) and 1.0×10^{17} cm^{-3} (dashed curve). The comparison of the complete displayed absorption spectra are presented in the inset by a vertical shift 1.0×10^4 cm^{-1}. The other parameters in the calculation are the same as those in Fig. 3.
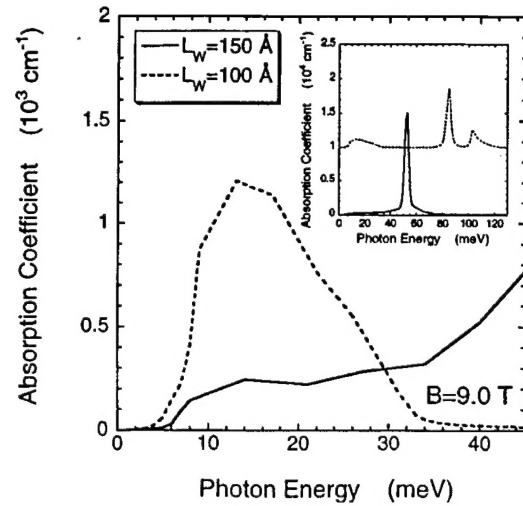

FIG. 9. The comparison of the enlarged low-energy part of the absorption spectra at $B=9.0$ T for $L_{W1}=L_{W2}=L_W=150$ Å (solid curve) and $L_{W1}=L_{W2}=L_W=100$ Å (dashed curve). The comparison of the complete displayed absorption spectra are presented in the inset by a vertical shift 1.0×10^4 cm^{-1}. The other parameters in the calculation are the same as those in Fig. 3.

Figure 8 presents the absorption spectra for different total electron densities, $n_{2D}=6\times10^{11}$ cm^{-2} and 3×10^{11} cm^{-2} at $B=9.0$ T. As n_{2D} is decreased, the previous population range between $0.1\leq k_y\leq1.5$ or $-1.5\leq k_y\leq-0.1$ in the main part of Fig. 2 will be reduced. This causes the revivals of the gap between the transition energies $E_{21}(k_y)$ and $E_{31}(k_y)$ and the gap between the transition energies $E_{31}(k_y)$ and $E_{41}(k_y)$. This is clearly seen as two dips (dashed curve) occurring around $\hbar\omega=40$ meV and 60 meV in the figure. Further, the many-body effects on the optical absorption will be reduced with the decrease of n_{2D}, causing the down shifting of the absorption peak. This reduction of the many-body effects is more easily seen in the transition from $E_1(k_y)$ to $E_3(k_y)$ since it gains the largest peak strength.

D. Modifications by well and middle-barrier widths

Figure 9 shows the absorption spectra for different well widths, $L_{W1}=L_{W2}=L_W=150$ Å and 100 Å with $L_B=20$ Å at $B=9.0$ T. As L_W decreases from 150 to 100 Å, the two-dimensional electron densities n_{2D}^1 and n_{2D}^2 in both quantum wells are reduced by $n_{2D}^1=n_{2D}^2=N_{3D}L_W$. Meanwhile, the energy levels $E_1(k_y)$ and $E_3(k_y)$ become less dispersive in the central region around $k_y=0$. This is because the "effective" B scales approximately as $B_{eff}\propto1/d$ according to Eq. (1). Here, $d=L_W+L_B$ is the center-to-center distance between the wells. $B=9.0$ T for $L_W=150$ Å is then equivalent to $B=6.35$ T for $L_W=100$ Å. As a result, the unpopulated island in the main part of Fig. 2 disappears. This shifts down the low-energy edge of the transition from $E_1(k_y)$ to $E_2(k_y)$. Further, the minima of the transition energy $E_{31}(k_y)$ is greatly pushed up due to the increased energy level separation ($\propto1/L_W^2$) for small L_W. It opens a very large gap between this transition energy and the transition energy $E_{21}(k_y)$ as seen in the inset, as well as an upward shifting of the peak position for the transition from $E_1(k_y)$ to $E_3(k_y)$. The decrease of L_W causes the revival of the gap between the

transition energies $E_{31}(k_y)$ and $E_{41}(k_y)$. It pushes up the peak positions for the transition from $E_1(k_y)$ to $E_4(k_y)$ and separates these two absorption peaks in the inset.

Figure 10 displays the absorption spectra for different middle-barrier widths, $L_B=20$ Å and 15 Å at $B=9.0$ T. As L_B decreases from 20 to 15 Å, the tunneling between the two quantum wells becomes stronger, and the energy level anticrossing is enlarged. As a result of the repulsion between the energy levels due to their enhanced anticrossing or the increase of the effective parallel magnetic field B_{eff} for small L_B, the unpopulated island in the main part of Fig. 2 disappears. This shifts down the low-energy edge of the transition
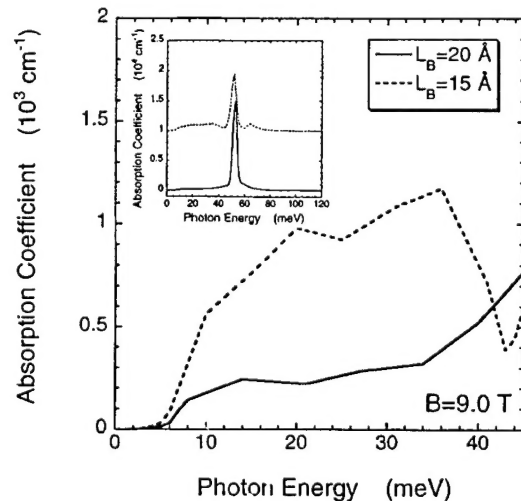

FIG. 10. The comparison of the enlarged low-energy part of the absorption spectra at $B=9.0$ T for $L_B=20$ Å (solid curve) and $L_B=15$ Å (dashed curve). The comparison of the complete displayed absorption spectra are presented in the inset by a vertical shift 1.0×10^4 cm^{-1}. The other parameters in the calculation are the same as those in Fig. 3.
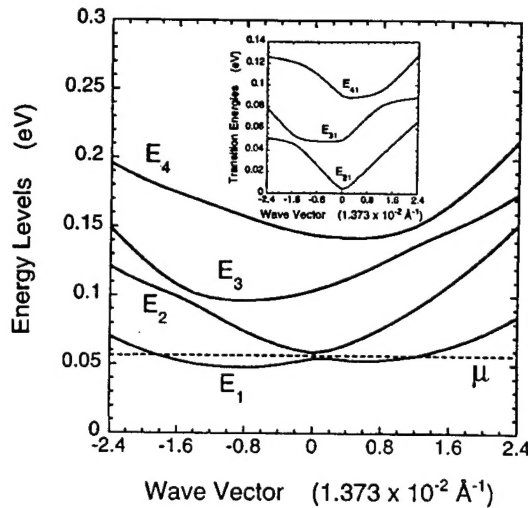
FIG. 11. The energy levels $E_j(k_y)$ with $j=1, 2, 3, 4$ as a function of the k_y at $B=9.0$ T for the asymmetric double quantum wells with with $L_{W1}=150$ Å and $L_{W2}=100$ Å. The dashed line represents μ which is the chemical potential of the system. The inset shows the transition energies $E_{j'j}(k_y)$ with $j'=2, 3, 4$, and $j=1$ as a function of k_y at $B=9.0$ T for the asymmetric double quantum wells. The other parameters in the calculation are the same as those in Fig. 3.
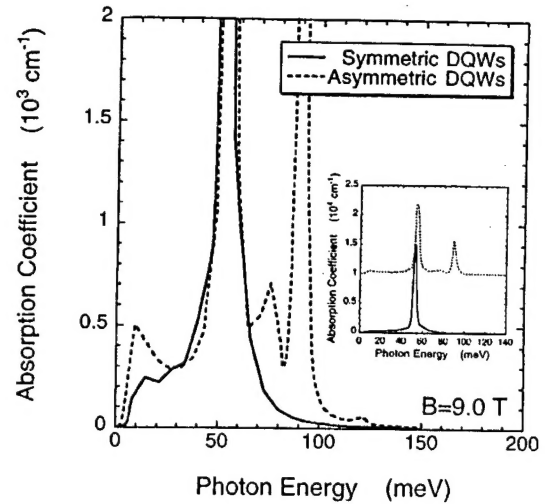

FIG. 12. The comparison of the absorption spectra with an amplified scale at $B=9.0$ T for the symmetric double quantum wells with $L_{W1}=L_{W2}=150$ Å (solid curve) and asymmetric double quantum wells with $L_{W1}=150$ Å and $L_{W2}=100$ Å (dashed curve). The comparison of the complete displayed absorption spectra are presented in the inset by a vertical shift 1.0×10^4 cm^{-1}. The other parameters in the calculation are the same as those in Fig. 3.

from $E_1(k_y)$ to $E_2(k_y)$. Meanwhile, it causes the revivals of the gap between the transition energies $E_{21}(k_y)$ and $E_{31}(k_y)$ and the gap between the transition energies $E_{31}(k_y)$ and $E_{41}(k_y)$ as seen in the inset. Further, the direct result of the level repulsion shifts down the peak for the transition from $E_1(k_y)$ to $E_3(k_y)$ and shifts up the peak for the transition from $E_1(k_y)$ to $E_4(k_y)$, simultaneously.

E. Difference between symmetric and asymmetric DQWs

Figure 11 shows the energy levels $E_j(k_y)$ as a function of k_y at $B=9.0$ T for the asymmetric DQWs with $L_{W1}=150$ Å, $L_{W2}=100$ Å, and $L_B=20$ Å. Compared with Fig. 2, a huge asymmetry is introduced to the dispersion between the positive and negative k_y regions in Fig. 11. As L_{W2} is decreased from 150 to 100 Å, the electron density in one of the quantum wells is reduced, which makes the previous unpopulated island in the symmetric DQWs go under the chemical potential sea and become populated. This explains the shifting down of the low-energy edge of the transition from $E_1(k_y)$ to $E_2(k_y)$ in the main part of Fig. 12. The inset shows the transition energies $E_{j'j}(k_y)$ as a function of k_y in which we find the minima of the transition energy $E_{41}(k_y)$ is pushed up by narrowing one of the quantum wells. This is the reason for the large separation between the two absorption peaks from the transitions $E_1(k_y)$ to $E_3(k_y)$ and $E_1(k_y)$ to $E_4(k_y)$ in the inset of Fig. 12. Further, from the asymmetric population of electron states in the range of $-1.8 \leq k_y \leq 1.2$ as shown in the main part of Fig. 11, it is easy to understand from the inset of the figure that the revival of the gap between the transition energies $E_{31}(k_y)$ and $E_{41}(k_y)$.

Figure 12 presents the comparison of the absorption spectra for symmetric DQWs with $L_{W1}=L_{W2}=150$ Å and asymmetric DQWs with $L_{W1}=150$ Å, $L_{W2}=100$ Å at B

$=9.0$ T. Here, $L_B=20$ Å for both the symmetric and asymmetric DQWs. As we go from symmetric to asymmetric DQWs, the low-energy edge of the transition from $E_1(k_y)$ to $E_2(k_y)$ is shifted down in the figure, as explained in the discussion of Fig. 11. Also, the gap between the transition energies $E_{31}(k_y)$ and $E_{41}(k_y)$ is opened, which is shown as the dip (dashed curve) at $\hbar\omega=80$ meV in the absorption spectrum for the asymmetric DQWs. This has been explained in the discussion of Fig. 11. From the inset, we find the absorption peak of the transition from $E_1(k_y)$ to $E_4(k_y)$ is pushed up and becomes well separated from the peak of the transition from $E_1(k_y)$ to $E_3(k_y)$, as explained in the discussion of Fig. 11. The flatlike dispersion in the transition energy $E_{41}(k_y)$ around $k_y=-1.8$, as shown in the inset of Fig. 11, gives rise to a large density-of-states which causes the "hump" around $\hbar\omega=120$ meV (dashed curve) in the main part of Fig. 12.

Figure 13 displays the square dipole moments $[F_{jj'}(k_y)]^2$ with $j=1$ and $j'=2, 3, 4$ for asymmetric DQWs at $B=9.0$ T. Compared with symmetric DQWs in the inset (reproduced from Fig. 4), a huge asymmetry in $[F_{jj'}(k_y)]^2$ between the positive and negative k_y regions is introduced in Fig. 13. $[F_{13}(k_y)]^2$ is no longer zero at $k_y=0$. Therefore, the transition from $E_1(k_y)$ to $E_3(k_y)$ is no longer forbidden at $k_y=0$. For $[F_{12}(k_y)]^2$, there exists a minima around $k_y=-1.0$ in Fig. 13. This corresponds to about $E_{21}(k_y)=30$ meV in the inset of Fig. 11, and is the reason for the occurrence of the dip (dashed curve) around $\hbar\omega=30$ meV in the main part of Fig. 12. For $[F_{13}(k_y)]^2$, there exists another minima around $k_y=0.2$ in Fig. 13. It corresponds to about $E_{31}(k_y)=55$ meV in the inset of Fig. 11, and explains the dip (dashed curve) seen around $\hbar\omega=65$ meV in the main part of Fig. 12 when we consider there is an additional zero cutoff of $[F_{13}(k_y)]^2$ at $k_y=-1.8$ corresponding to about $E_{31}(k_y)$
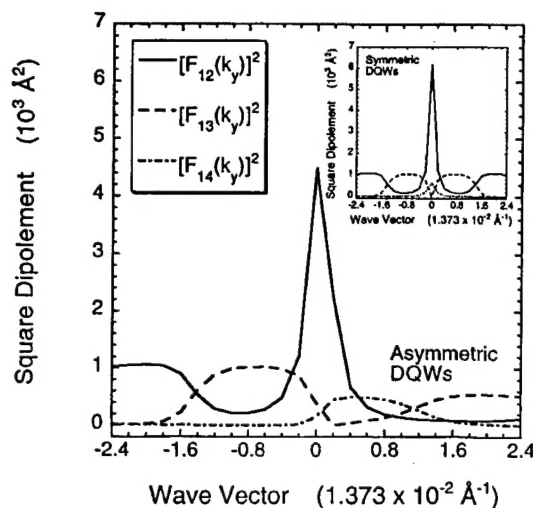
FIG. 13. The square dipole moments $[F_{12}(k_y)]^2$ (solid curve), $[F_{13}(k_y)]^2$ (dashed curve), and $[F_{14}(k_y)]^2$ (dashed-dotted curve) as a function of k_y at $B = 9.0$ T for the asymmetric double quantum wells with $L_{W1} = 150$ Å and $L_{W2} = 100$ Å. The inset displays the correspondent square dipole moments $[F_{12}(k_y)]^2$, $[F_{13}(k_y)]^2$, and $[F_{14}(k_y)]^2$ as a function of k_y reproduced from the main part of Fig. 4 for the symmetric double quantum wells with $L_{W1} = L_{W2} = 150$ Å. The other parameters in the calculation are the same as those in Fig. 3.

$= 60$ meV. A similar saturation of the square dipole moments at large $|k_y|$ in the inset is also found in the main part of the figure.

V. CONCLUSIONS AND REMARKS

In conclusion, by using the density-functional theory the electron eigenstates in the double quantum well under a parallel magnetic field are calculated accurately including the Coulomb interaction between electrons, z dependence of electron effective mass and dielectric constant, nonparabolic effect, and a static electric field. The self-consistent-field theory is applied to calculate the optical intersubband absorption spectrum including the many-body effects. The effects of magnetic field, temperature, electron density, well and middle-barrier widths, quantum-well symmetry, and electric field on the absorption spectrum have been studied extensively and their physical origins have been elucidated.

From the numerical results presented in this article, we have found that both the band-width and the absorption strength of the windowlike infrared optical absorption from the ground state to the first excited state can be engineered to

a very great extent by varying the parallel magnetic field, temperature, electron density, well width, middle-barrier width, double-quantum-well symmetry, and electric field. This provides us with an unconventional approach for designing a tunable wide-band quantum well infrared photodetector.

[1] A. Köck, E. Gornik, G. Abstreiter, G. Böhm, M. Walther, and G. Weimann, Appl. Phys. Lett. **60**, 2011 (1992).

[2] M. C. Chen and M. J. Bevan, J. Appl. Phys. **78**, 4787 (1995).

[3] C. J. Chen, K. K. Choi, M. Z. Tidrow, and D. C. Tsui, Appl. Phys. Lett. **68**, 1446 (1996).

[4] Y. Zhang, D. S. Jiang, J. B. Xia, L. Q. Cui, C. Y. Song, and Z. Q. Zhou, Appl. Phys. Lett. **68**, 2114 (1996).

[5] I. Gravé, A. Shakouri, N. Kuze, and A. Yariv, Appl. Phys. Lett. **60**, 2362 (1992).

[6] K. L. Tsai, K. H. Chang, C. P. Lee, K. F. Huang, J. S. Tsang, and H. R. Chen, Appl. Phys. Lett. **62**, 3504 (1993).

[7] S. R. Parihar, S. A. Lyon, M. Santos, and M. Shayegan, Appl. Phys. Lett. **55**, 2417 (1989).

[8] K. K. Choi, B. F. Levine, C. G. Bethea, J. Walker, and R. J. Malik, Phys. Rev. B **39**, 8029 (1989).

[9] V. Berger, N. Vodjdani, P. Bois, B. Vinter, and S. Delaitre, Appl. Phys. Lett. **61**, 1898 (1992).

[10] Y. Huang and C. Lien, J. Appl. Phys. **77**, 3433 (1995).

[11] H. Schneider, C. Schönbeinm, and Bihlmann, Appl. Phys. Lett. **68**, 1832 (1996).

[12] K. Kheng, M. Ramsteiner, H. Schneider, J. D. Ralston, F. Fuchs, and P. Koidl, Appl. Phys. Lett. **61**, 666 (1992).

[13] Y. H. Wang and S. S. Li, Appl. Phys. Lett. **62**, 93 (1993).

[14] D. H. Huang and M. O. Manasreh, Phys. Rev. B **54**, 5620 (1996).

[15] D. H. Huang and M. O. Manasreh, J. Appl. Phys. **80**, 6045 (1996).

[16] H. Haug and S. W. Koch, in *Quantum Theory of the Optical and Electronic Properties of Semiconductors*, edited by H. Haug and S. W. Koch (World Scientific, Singapore, 1990), Chap. 17.

[17] J. A. Simmons, S. K. Lyo, N. E. Harff, and J. F. Klem, Phys. Rev. Lett. **73**, 2256 (1994).

[18] S. K. Lyo, Phys. Rev. B **50**, 4965 (1994).

[19] I. S. Millard, N. K. Patel, C. Foden, E. H. Linfield, D. A. Ritchie, G. A. C. Jones, and M. Pepper, J. Phys.: Condens. Matter **9**, 1079 (1997).

[20] T. Jungwirth, T. S. Lay, L. Smrčka, and M. Shayegan, Phys. Rev. B **56**, 1029 (1997).

[21] S. K. Lyo, in *Infrared Applications of Semiconductors—Material, Processing and Devices*, edited by M. O. Manasreh, T. H. Myers, and F. H. Julien (Mater. Res. Soc. Proc. 450, Pittsburgh, PA, 1997), pp. 189–194.

[22] S. Adachi, J. Appl. Phys. **53**, R1 (1985).

[23] L. Hedin and B. I. Lundqvist, J. Phys. C **4**, 2064 (1971).

[24] A. C. Tselis and J. J. Quinn, Phys. Rev. B **29**, 3318 (1984).

[25] D. H. Huang, G. Gumbs, V. Fessatidis, and N. J. M. Horing, J. Phys.: Condens. Matter **6**, 9219 (1994).